Electronic Supplementary Information

Hierarchical architecture of WS_2 nanosheet on graphene framework with enhanced electrochemical properties for lithium storage and hydrogen evolution

Guowei Huang,[a] Hao Liu,[b] Shengping Wang,[a] Xi Yang,[a] Binhong Liu,[b] Hongzheng Chen[a] and Mingsheng Xu*[a]

[a]*State Key Laboratory of Silicon Materials, MOE Key Laboratory of Macromolecular Synthesis and Functionalization, Department of Polymer Science and Engineering, Zhejiang University, Hangzhou 310027, P. R. China. E-mail: msxu@zju.edu.cn*
[b]*School of Materials Science and Engineering, Zhejiang University, Hangzhou 310027, P. R. China*

Experimental Section

Materials Characterization: The structure features of GO nanosheets were investigated using a Veeco Multimode atomic force microscope (AFM) in the tapping mode. Sample was prepared by drop-drying from a GO suspension (1 mg mL^{-1}) onto a fresh mica slide. X-ray diffraction (XRD) was carried out using a Rigaku D/Max Ultima IV X-ray powder diffractometer operating at 40 kV, 40 mA for Cu Kα radiation (λ = 1.5418 Å). Samples were prepared by drop-drying a water suspension of the product onto glass substrates. Raman spectra were taken using a Raman spectrometer with a laser excitation wavelength of 532 nm. To calibrate the wavenumber, the Si peak at 520 cm^{-1} was used as a reference. The morphology and composition of the WS_2/3DG hybrids were characterized using a Hitachi S-4800 field emission scanning electron microscope (FESEM) and a FEI TECNAI G2 F20-TWIN transmission electron microscope (TEM) equipped with Energy dispersive X-ray spectroscope (EDS). Thermogravimetric analysis (TGA) was performed using a Q500 thermoanalyzer with a heating rate of 10 °C min^{-1} in air atmosphere. Nitrogen adsorption-desorption isotherm measurements were recorded using an AUTOSORB-IQ2-MP to study

specific surface area. Before analysis, the samples were degassed at room temperature to avoid further thermal reduction or decomposition of 3DG.[1] X-ray photoelectron spectroscopy (XPS) was performed using ESCALAB 250Xi system with Al Kα as the source and the C 1s peak at 284.8 eV as an internal standard.

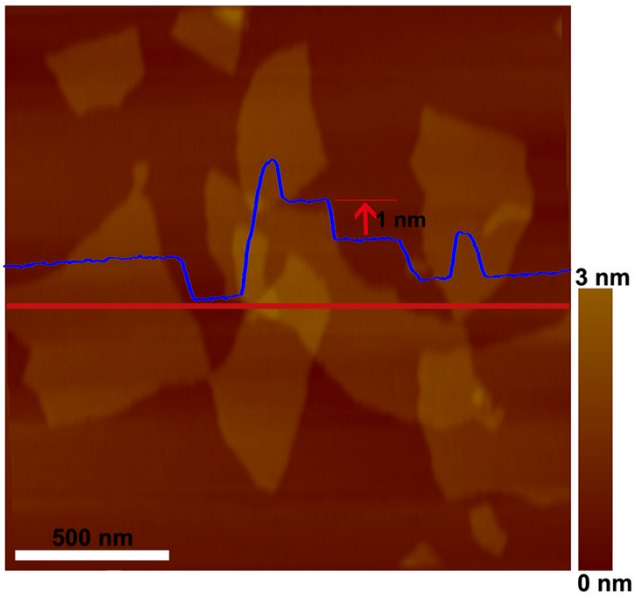

Fig. S1 AFM image of GO nanosheets, suggesting uniform thickness of about 1 nm.

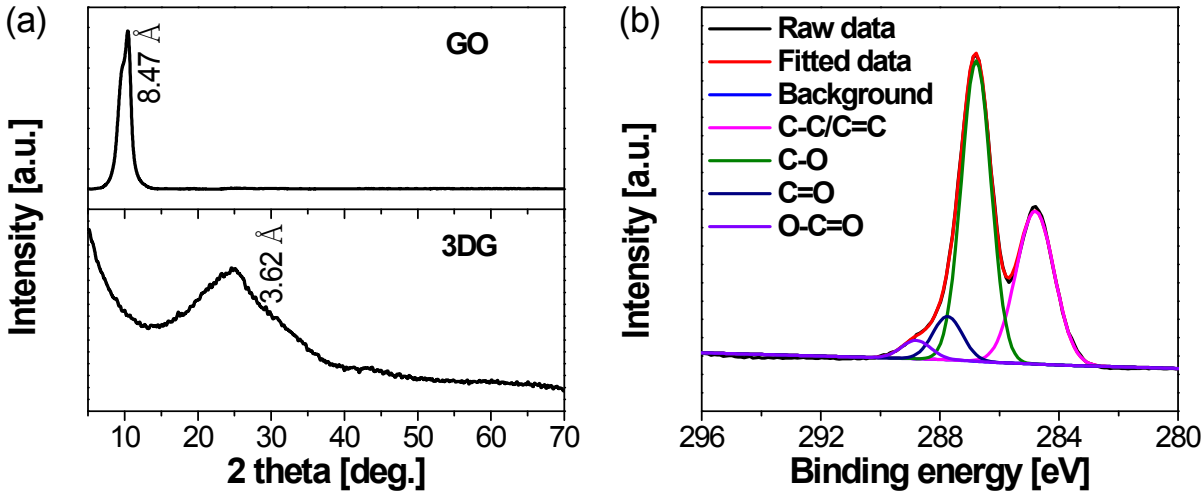

Fig. S2 a) XRD patterns of GO and 3DG. b) C1s XPS of GO.

XRD was carried out with a scan rate of 5° min^{-1} in the range of 5-80°. The diffraction peak at 10.4° of GO implies an interlayer spacing of 8.47 Å, which may result from the water molecules trapped between oxygen-containing functional groups on GO sheets.[2]

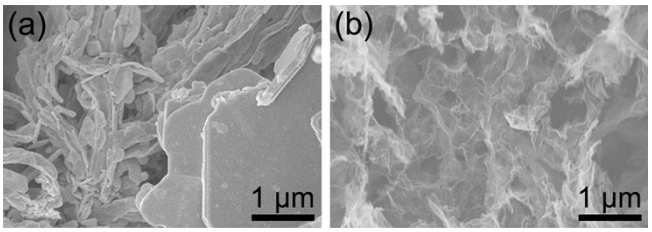

Fig. S3 SEM images of a) bulk WS_2 powder and b) 3DG.

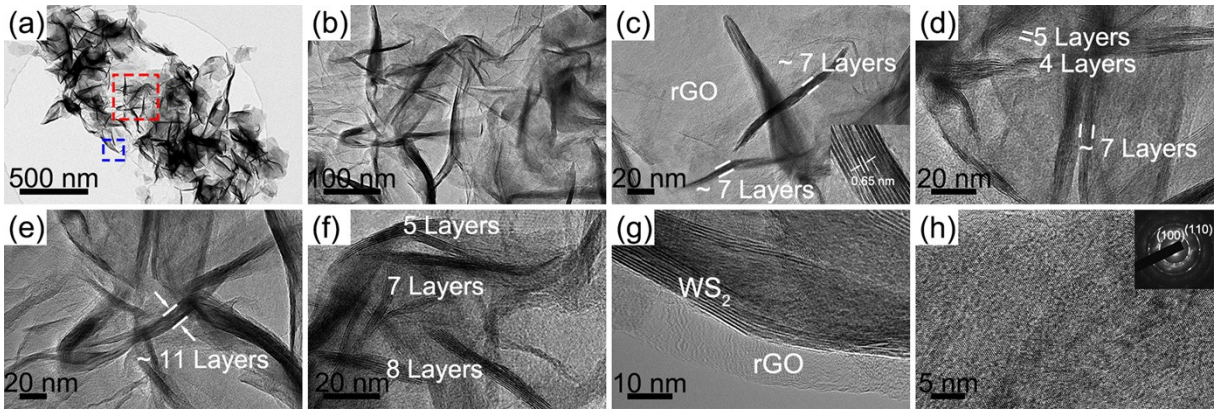

Fig. S4 TEM images of annealed WS_2/3DG. a) As-prepared annealed WS_2/3DG and b) the magnified image of the area marked by red square in (a). c-f) The high-resolution images of (b). The inset in (c) indicates the interlayer spacing of WS_2 is 0.65 nm. g-h) The high-resolution images of the area marked by blue square in (a). The inset in (h) shows the diffraction pattern of 2H-WS_2.

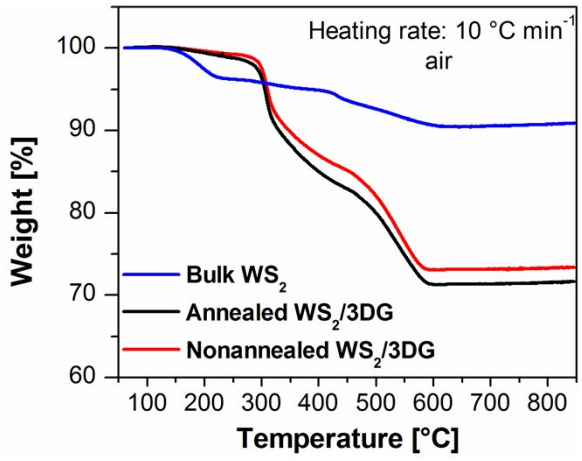

Fig. S5 Thermogravimetric analysis (TGA) curves of bulk WS_2, annealed WS_2/3DG, and nonannealed WS_2/3DG.

To determine the weight percentage of WS_2 in WS_2/3DG composites, thermogravimetric analysis (TGA) was performed on bulk WS_2 and WS_2/3DG nanocomposites (Fig. S5). The content of WS_2 in the annealed sample can be calculated from the equation below

WS_2 (wt%) = 100% * (wt% of composite sample at 800 °C) / (wt% of bulk WS_2 at 800 °C)

It is ascertained that there is approximately 21.1 wt% rGO and 78.9 wt% WS_2 in the annealed WS_2/3DG sample. But for nonannealed sample, it is difficult to resolve the weight percentage of WS_2 because of the oxygen incorporation in this circumstance.

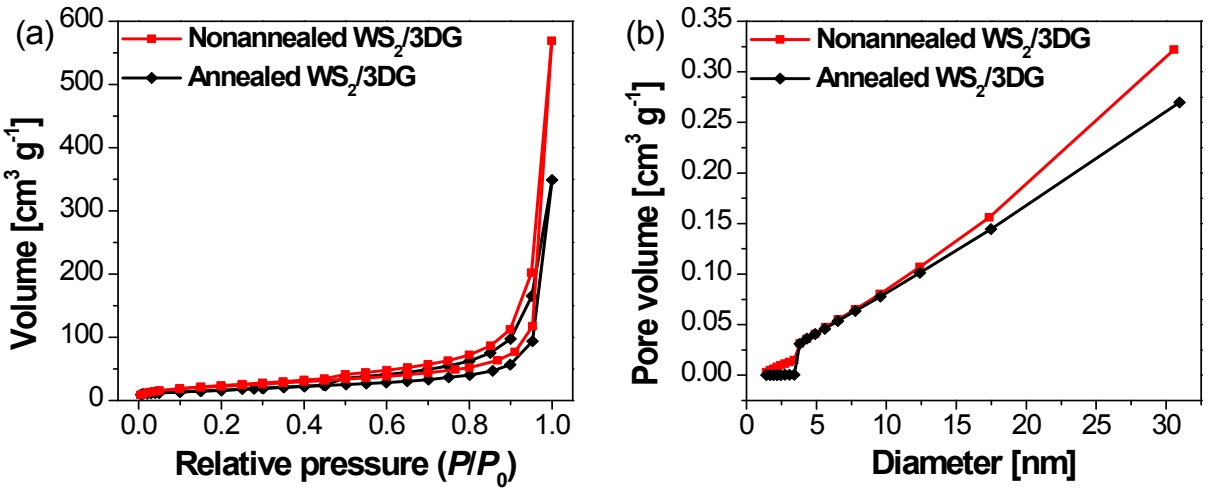

Fig. S6 a) Nitrogen adsorption/desorption isotherms of nonannealed WS_2/3DG and annealed WS_2/3DG, possessing specific surface areas of 82.3 m^2 g^{-1} and 59.9 m^2 g^{-1}, respectively. b) Pore size distributions of both samples in the range of 1-30 nm.

The porous nature of WS_2/3DG macrostructures was further characterized by the nitrogen physisorption measurements (Fig. S6). As mentioned in the Experimental Section, the samples were degassed at room temperature to avoid thermal reduction or decomposition of 3DG. Therefore, their specific surface areas could be underestimated because of incomplete degassing before surface analysis. Indeed, it is more accurate and reliable to determine the intrinsic specific surface area via methylene blue (MB) dye adsorption method under the pristine wet conditions of WS_2/3DG.[1,3] Nevertheless, the results definitely demonstrate higher BET surface area for nonannealed WS_2/3DG. Barrett-Joyner-Halenda (BJH) calculations reveal that the pore size distributions of both composites are in the range of 1-30 nm, except for the conspicuous macropores presented in the SEM images.

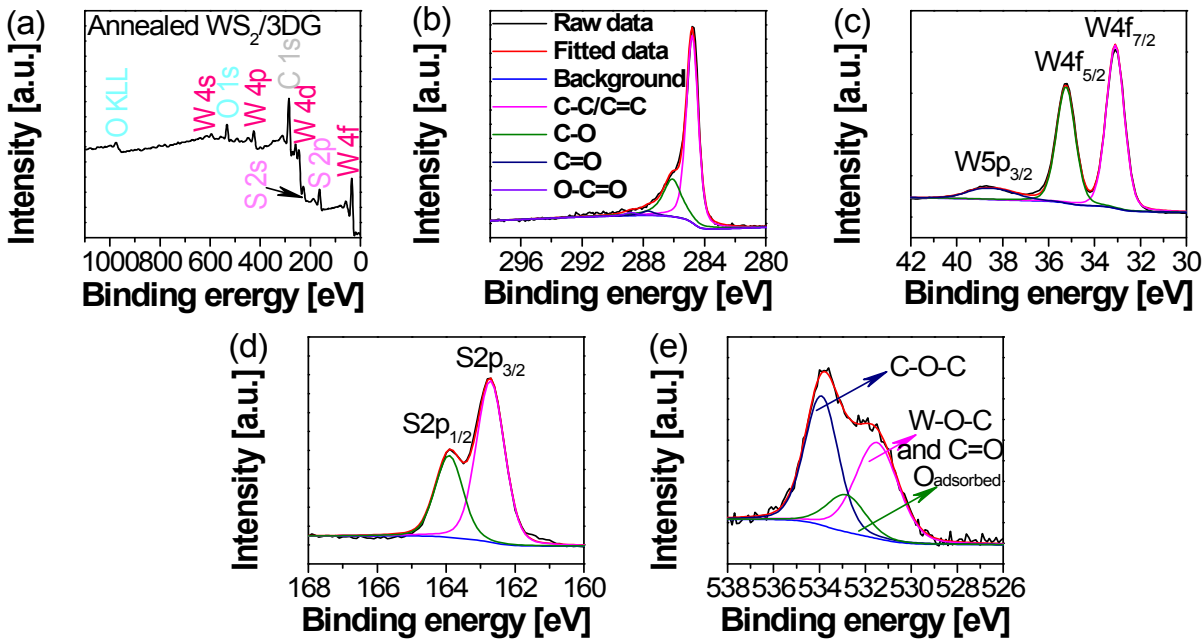

Fig. S7 XPS patterns of annealed WS_2/3DG sample: a) survey and high-resolution of b) C1s, c) W4f, d) S2p, and e) O1s.

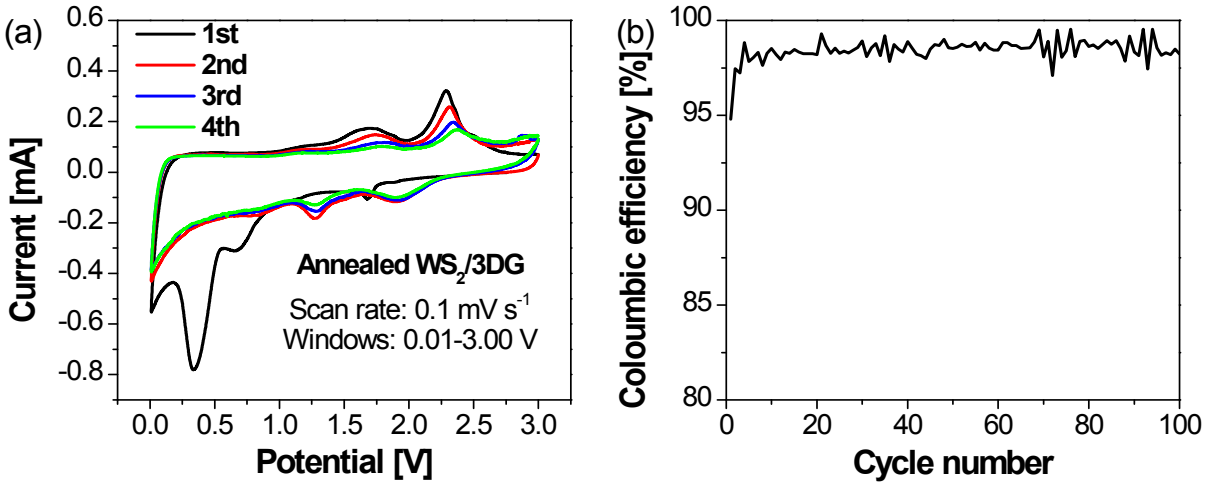

Fig. S8 a) Cyclic voltammogram of annealed WS_2/3DG at a scan rate of 0.1 mV s^{-1} for four cycles. b) Coulombic efficiency of nonannealed WS_2/3DG composite cycled at a current density of 100 mA g^{-1}.

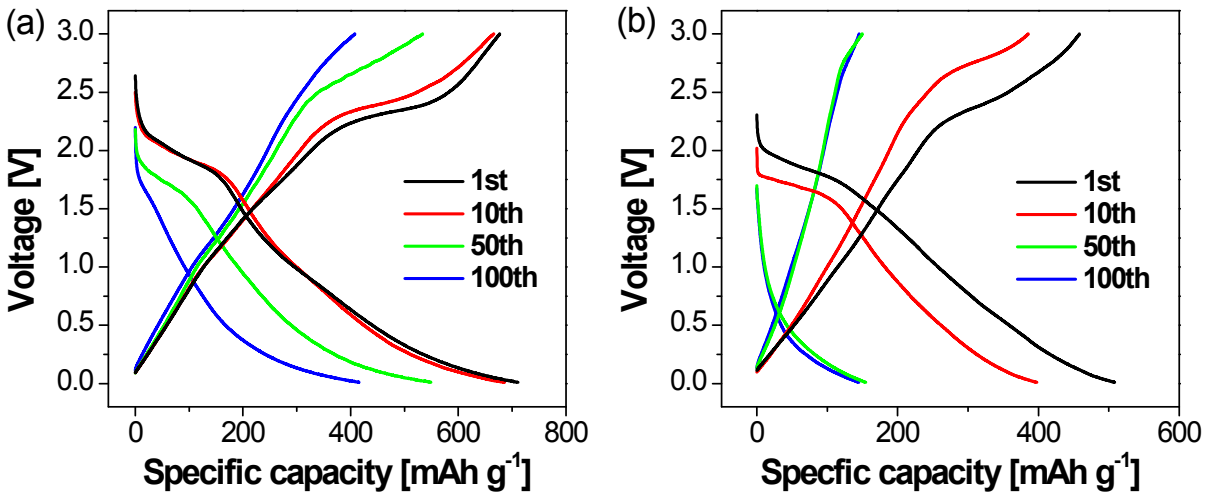

Fig. S9 Discharge-charge voltage profiles of a) annealed WS_2/3DG and b) bulk WS_2 during cycling at a current density of 100 mA g^{-1}.

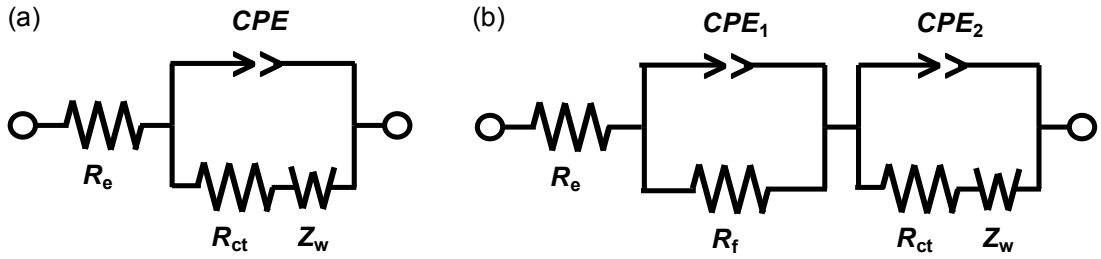

Fig. S10 Randles equivalent circuits for nonannealed WS_2/3DG, annealed WS_2/3DG, and bulk WS_2 electrode/electrolyte interface a) before cycling and b) after 100 cycles. R_e and *CPE* are related to the electrolyte resistance and corresponding constant phase element. R_f and R_{ct} are the resistance of SEI film and charge-transfer, respectively, while Z_w represents the Warburg impedance associated with lithium ion diffusion.

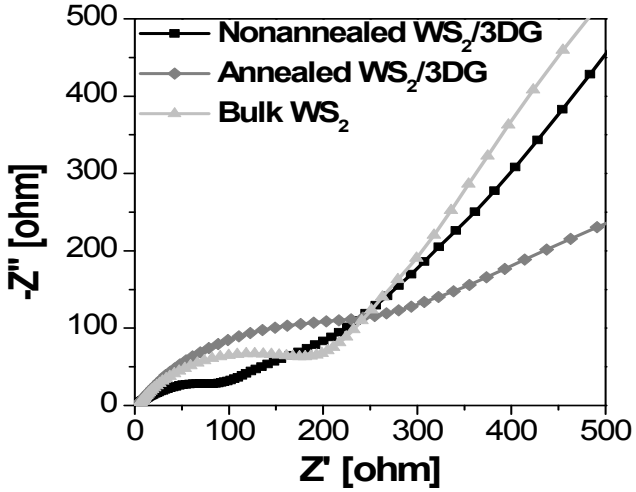

Fig. S11 Nyquist plots of nonannealed WS_2/3DG, annealed WS_2/3DG, and bulk WS_2 electrodes obtained at open potential after 100 cycles.

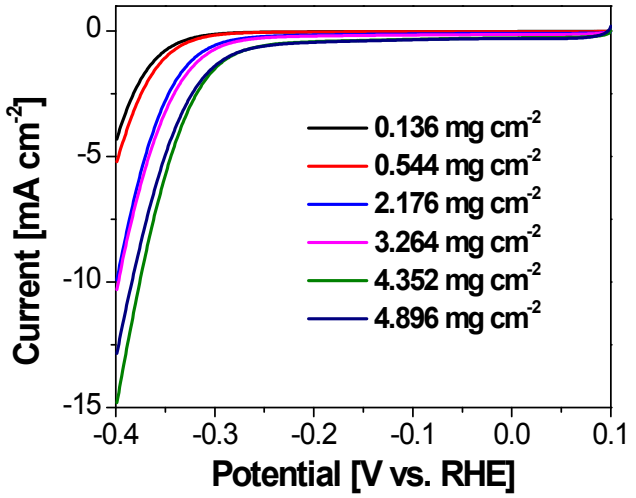

Fig. S12 Polarization curves of nonannealed WS_2/3DG powder at different loading weight.

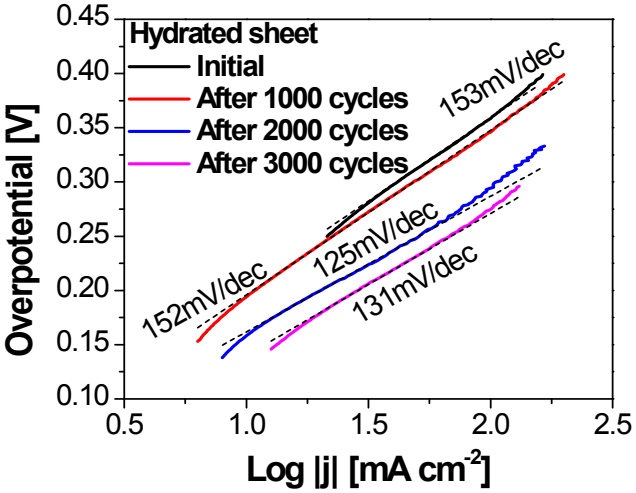

Fig. S13 Tafel plots of hydrated sheet before and after different CV cycles.

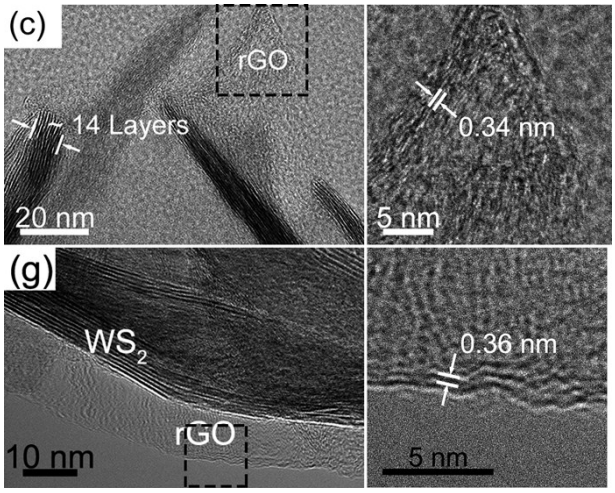

Fig. S14 Corresponding magnified HRTEM images of Fig. 3c and Fig. S4g.

The above figure shows that the interlayer spacings of rGO in both the WS_2/3DG composites are estimated to be close to the (002) lattice distance in hexagonal graphite (0.34 nm).

Table S1 Elemental analyses of nonannealed WS_2/3DG and annealed WS_2/3DG

Sample		Nonannealed WS_2/3DG	Annealed WS_2/3DG
Atom% of oxygen		12.77	10.62
Atom ratio of W/S	by XPS	1:2.14	1:2.15
	by EDS	1:1.91	1:2.01
W species (atom%)	$W^{(IV)}S_2$	61.2	100
	$W^{(IV)}O_2$	20.2	-
	$W^{(VI)}O_3$	18.6	-
O species (atom%)	W-O	7.6	-
	W-O-C	9.8	41.4
	$O_{adsorbed}$	47.3	14.5
	C-O-C	35.3	44.1

It is worth pointing out that the data in the above table were obtained on average from several measurements of the same sample, especially concerning the extreme surface sensitivity of XPS characterization. In contrast with the annealed WS_2/3DG, the nonannealed counterpart is prone to adsorb adventitious oxygen components (47.3% $O_{adsorbed}$) from the atmosphere, which may render itself more susceptible to oxidation as indicated in the manuscript. Consequently, the ratios of W species would deviate from the exact values of this composite. For instance, some part of the $W^{(IV)}S_2$ species could be assigned as the components of $W^{(IV)}O_2$ species. Therefore, it is more appropriate to estimate the ratios of W species through the EDX results rather than the XPS results. From this perspective, the oxygen-incorporated WS_2 nanosheets in the nonannealed composite can be tentatively derived as $WS_{1.91}O_{0.09}$, that is, approximately 5% oxygen incorporated in the lattice of intrinsic WS_2 nanosheets.

Table S2 Summary of discharge capacity of various WS_2-based anodes.

WS_2-based anode	Discharge capacity [mAh g^{-1}]	Voltage range [V]	Current density [mA g^{-1}]	Reference
Nonannealed WS_2/3DG	**766 (after 100 cycles)**	**0.01-3.0**	**100**	**This work**
WS_2/rGO paper	697.7 (after 100 cycles)	0.01-3.0	100	4
Freeze-dried WS_2/rGO	647 (after 80 cycles)	0.01-3.0	350	5
WS_2-rGO composite	451 (after 50 cycles)	0.01-3.0	100	6
Few-layer WS_2/N-doped rGO	830 (after 100 cycles)	0.01-3.0	100	7
WS_2 nanotube/3DG	500.2 (after 100 cycles)	0.01-3.0	100	8
WS_2/SWCNT paper	861.6 (after 50 cycles)	0.01-3.0	100	9
Amorphous WS_2/carbon composite	555 (after 50 cycles)	0.001-3.0	100	10

Table S3 Impedance parameters derived from corresponding equivalent circuit modal for different electrodes.

Sample	**R_e (Ω)**	**R_f (Ω)**	**R_{ct} (Ω)**
Nonannealed WS_2/3DG (before cycling)	2.9	-	42.8
Annealed WS_2/3DG (before cycling)	2.5	-	94.9
Bulk WS_2 (before cycling)	2.0	-	136.4
Nonannealed WS_2/3DG (100th)	2.3	98.3	29.7
Bulk WS_2 (100th)	4.2	103.0	55.9

Table S4 A brief survey of WS_2 and MoS_2 HER electrocatalysts reported in literature.

Catalyst	Catalyst loading [mg cm^{-2}]	2D/3D[a)]	Onset overpotential [mV][b)]	Tafel slope [mV/dec]	η@300V [mA cm^{-2}]	Reference
WS_2/3DG	**>10**	**3D**	**~75**	**131**	**137**	**This work**
Vertical WS_2 nanosheets on carbon cloth	1.5	3D	~150	105	~30	11
Porous WS_2 thin film on W foil	~0.08	3D	~100	67	~22	12
WS_2/rGO nanosheets	0.4	2D	150-200	58	23	13
Mono-layered WS_2/rGO nanosheets	~0.562	2D	~100	52	N/A	14
Ultrathin WS_2 nanoflakes	0.35	2D	100	48	N/A	15
Strained chemically exfoliated WS_2 nanosheets	0.1-0.2	2D	30-60	~60	26	16
Metallic WS_2 nanosheets	1±0.2	2D	75	70	N/A	17
Amorphous MoS_x NPs coated sponge	N/A	3D	~0	185	232	18

Amorphous MoS_x NPs on 3DG/Ni	8.09	3D	109-141	42.8	~140	19
Porous MoS_2 thin film on Mo foil	N/A	3D	150-200	50	18.6	20
Defect-rich ultrathin MoS_2 nanosheets	0.285	2D	120	50	70	21
Oxygen-incorporated MoS_2 nanosheets	0.285	2D	120	55	126.5	22
Vertical MoS_2 nanosheets on amorphous carbon	0.28	2D	80	40	~160	23
Vertical single-layered MoS_2 on N-doped carbon nanofibers	0.79	2D	30	38	~70	24
MoS_2 NPs on mesoporous grapheme foams	0.21	2D	~100	~42	N/A	25

[a)] 2D represents that the working electrode was made by casting on the glass carbon electrode, while 3D electrode works straightly; [b)] All potentials were converted to the reversible hydrogen electrode (RHE) scale.

References

[S1] S. H. Aboutalebi, R. Jalili, D. Esrafilzadeh, M. Salari, Z. Gholamvand, S. A. Yamini, K. Konstantinov, R. L. Shepherd, J. Chen, S. E. Moulton, P. C. Innis, A. I. Minett, J. M. Razal and G. G. Wallace, *ACS Nano* 2014, **8**, 2456.

[S2] A. M. Abdelkader, *J. Mater. Chem. A* 2015, **3**, 8519.

[S3] Y. X. Xu, Z. Y. Lin, X. Zhong, B. Papandrea, Y. Huang and X. F. Duan, *Angew. Chem., Int. Ed.* 2015, **54**, 5345.

[S4] Y. Liu, W. Wang, Y. W. Wang and X. S. Peng, *Nano Energy* 2014, **7**, 25.

[S5] X. D. Xu, C. S. Rout, J. Yang, R. G. Cao, P. Oh, H. S. Shin and J. Cho, *J. Mater. Chem. A* 2013, **1**, 14548.

[S6] K. Shiva, H. S. S. Ramakrishna Matte, H. B. Rajendra, A. J. Bhattacharyya and C. N. R. Rao, *Nano Energy* 2013, **2**, 787.

[S7] D. Y. Chen, G. Ji, B. Ding, Y. Ma, B. H. Qu, W. X. Chen and J. Y. Lee, *Nanoscale* 2013, **5**, 7890.

[S8] R. J. Chen, T. Zhao, W. P. Wu, F. Wu, L. Li, J. Qian, R. Xu, H. M. Wu, H. M. Albishri, A. S. Al-Bogami, D. A. El-Hady, J. Lu and K. Amine, *Nano Lett.* 2014, **14**, 5899.

[S9] Y. Liu, W. Wang, H. B. Huang, L. Gu, Y. W. Wang and X. S. Peng, *Chem. Commun.* 2014, **50**, 4485.

[S10] S. H. Choi, S. J. Boo, J. H. Lee and Y. C. Kang, *Sci. Rep.* 2014, **4**, 5755.

[S11] Y. Yan, B. Y. Xia, N. Li, Z. C. Xu, A. Fisher and X. Wang, *J. Mater. Chem. A* 2014, **3**, 131.

[S12] H. L. Fei, Y. Yang, X. J. Fan, G. Wang, G. D. Ruan and J. M. Tour, *J. Mater. Chem. A* 2015, **3**, 5798.

[S13] J. Yang, D. Voiry, S. J. Ahn, D. Kang, A. Y. Kim, M. Chhowalla and H. S. Shin, *Angew. Chem., Int. Ed.* 2013, **52**, 13751.

[S14] J. Zhang, Q. Wang, L. H. Wang, X. A. Li and W. Huang, *Nanoscale* 2015, **7**, 10391.

[S15] L. Cheng, W. J. Huang, Q. F. Gong, C. H. Liu, Z. Liu, Y. G. Li and H. J. Dai, *Angew. Chem., Int. Ed.* 2014, **53**, 7860.

[S16] D. Voiry, H. Yamaguchi, J. W. Li, R. Silva, D. C. Alves, T. Fujita, M. W. Chen, T. Asefa, V. B. Shenoy, G. Eda and M. Chhowalla, *Nat. Mater.* 2013, **12**, 850.

[S17] M. A. Lukowski, A. S. Daniel, C. R. English, F. Meng, A. Forticaux, R. J. Hamers and S. Jin, *Energy Environ. Sci.* 2014, **7**, 2608.

[S18] Y. H. Chang, F. Y. Wu, T. Y. Chen, C. L. Hsu, C. H. Chen, F. Wiryo, K. H. Wei and C. Y. Chiang, L. J. Li, *Small* 2014, **10**, 895.

[S19] Y. H. Chang, C. T. Lin, T. Y. Chen, C. L. Hsu, Y. H. Lee, W. J. Zhang, K. H. Wei and L. J. Li, *Adv. Mater.* 2013, **25**, 756.

[S20] Y. Yang, H. L. Fei, G. D. Ruan, C. S. Xiang and J. M. Tour, *Adv. Mater.* 2014, **26**, 8163.

[S21] J. F. Xie, H. Zhang, S. Li, R. X. Wang, X. Sun, M. Zhou, J. F. Zhou, X. W. Lou and Y. Xie, *Adv. Mater.* 2013, **25**, 5807.

[S22] J. F. Xie, J. J. Zhang, S. Li, F. Grote, X. D. Zhang, H. Zhang, R. X. Wang, Y. Lei, B. C. Pan and Y. Xie, *J. Am. Chem. Soc.* 2013, **135**, 17881.

[S23] X. Zhao, H. Zhu and X. R. Yang, *Nanoscale* 2014, **6**, 10680.

[S24] H. Zhu, M. L. Du, M. Zhang, M. L. Zou, T. T. Yang, S. L. Wang, J. M. Yao and B. C. Guo, *Chem. Commun.* 2014, **50**, 15435.

[S25] L. Liao, J. Zhu, X. J. Bian, L. N. Zhu, M. D. Scanlon, H. H. Girault and B. H. Liu, *Adv. Funct. Mater.* 2013, **23**, 5326.